Chinese Journal of Natural Medicines

Taohe Chengqi decoction inhibits PAD4–mediated neutrophil extracellular traps and mitigates acute lung injury induced by sepsis

Mengting Xie, Xiaoli Jiang, Weihao Jiang, Lining Yang, Xiaoyu Jue, Yunting Feng, Wei Chen, Shuangwei Zhang, Bin Liu, Zhangbin Tan, Bo Deng, Jingzhi Zhang

Citation: Mengting Xie, Xiaoli Jiang, Weihao Jiang, Lining Yang, Xiaoyu Jue, Yunting Feng, Wei Chen, Shuangwei Zhang, Bin Liu, Zhangbin Tan, Bo Deng, Jingzhi Zhang, Taohe Chengqi decoction inhibits PAD4–mediated neutrophil extracellular traps and mitigates acute lung injury induced by sepsis, Chinese Journal of Natural Medicines, 2025, 23(10), 1195–1209. doi: 10.1016/S1875–5364(25)60874–0.

View online: https://doi.org/10.1016/S1875–5364(25)60874–0

Chinese Journal of Natural Medicines 23 (2025) 1195-1209

Contents lists available at ScienceDirect

Chinese Journal of Natural Medicines

journal homepage: www.cjnmcpu.com/

Original article

Taohe Chengqi decoction inhibits PAD4-mediated neutrophil extracellular traps and mitigates acute lung injury induced by sepsis

Mengting Xie[a,Δ], Xiaoli Jiang[a,Δ], Weihao Jiang[a,Δ], Lining Yang[a], Xiaoyu Jue[a], Yunting Feng[a], Wei Chen[b], Shuangwei Zhang[a], Bin Liu[a], Zhangbin Tan[a,*], Bo Deng[a,*], Jingzhi Zhang[a,*]

[a] *Department of Traditional Chinese Medicine, Guangzhou Institute of Cardiovascular Disease, State Key Laboratory of Respiratory Disease, Institute of Integration of Traditional and Western Medicine of Guangzhou Medical University, the Second Affiliated Hospital of Guangzhou Medical University, Guangzhou 510260, China*

[b] *The First Clinical School of Guangzhou Medical University, Guangzhou Medical University, Guangzhou 510260, China*

ARTICLE INFO

Article history:
Received 19 August 2024
Revised 3 December 2024
Accepted 5 December 2024
Available online 20 October 2025

Keywords:
Acute lung injury
Cecum ligation and puncture
Neutrophil extracellular traps
PAD4

ABSTRACT

Acute lung injury (ALI) is a significant complication of sepsis, characterized by high morbidity, mortality, and poor prognosis. Neutrophils, as critical intrinsic immune cells in the lung, play a fundamental role in the development and progression of ALI. During ALI, neutrophils generate neutrophil extracellular traps (NETs), and excessive NETs can intensify inflammatory injury. Research indicates that Taohe Chengqi decoction (THCQD) can ameliorate sepsis-induced lung inflammation and modulate immune function. This study aimed to investigate the mechanisms by which THCQD improves ALI and its relationship with NETs in sepsis patients, seeking to provide novel perspectives and interventions for clinical treatment. The findings demonstrate that THCQD enhanced survival rates and reduced lung injury in the cecum ligation and puncture (CLP)-induced ALI mouse model. Furthermore, THCQD diminished neutrophil and macrophage infiltration, inflammatory responses, and the production of pro-inflammatory cytokines, including interleukin-1β (IL-1β), IL-6, and tumor necrosis factor α (TNF-α). Notably, subsequent experiments confirmed that THCQD inhibits NET formation both *in vivo* and *in vitro*. Moreover, THCQD significantly decreased the expression of peptidyl arginine deiminase 4 (PAD4) protein, and molecular docking predicted that certain active compounds in THCQD could bind tightly to PAD4. PAD4 overexpression partially reversed THCQD's inhibitory effects on PAD4. These findings strongly indicate that THCQD mitigates CLP-induced ALI by inhibiting PAD4-mediated NETs.

1. Introduction

Sepsis, a potentially fatal and severe disease syndrome, results from an abnormal host response to infection [1-3]. Its high mortality rate and extensive health impact establish sepsis as a major global public health challenge. Among sepsis complications, acute lung injury (ALI) occurs frequently [4], increasing patient mortality and substantially extending intensive care unit stays. ALI is characterized by alveolar-capillary membrane damage, resulting in pulmonary edema and impaired gas exchange, with inflammatory response and immune cell activation serving as key pathological factors [5]. The inflammatory cells involved in ALI primarily include neutrophils, macrophages, lymphocytes, and natural killer cells, which facilitate the inflammatory response by releasing pro-inflammatory factors, leading to substantial inflammatory cell accumulation and infiltration in lung tissue [6]. Neutrophils, as crucial intrinsic immune cells in the lungs, are essential to ALI development and progression. During ALI, neutrophils produce neutrophil extracellular traps (NETs), comprising deoxyribonucleic acids (DNAs), histones, and anti-microbial proteins. While NETs serve an important function in trapping and eliminating pathogens, their excessive formation and inadequate clearance contribute to various inflammatory diseases, including ALI [7, 8].

Excessive NET generation and accumulation can directly damage lung tissue. Research indicates that NETs exacerbate inflammatory injury in ALI through cGAS-STING pathway activation [9, 10]. The histones and free DNA within NETs activate both exogenous and endogenous coagulation pathways, leading to microthrombosis and microcirculatory disturbances. These effects trigger endothelial and epithelial cell death, alveolar congestion, and barrier function loss [11]. Furthermore, excessive NET formation not only directly damages lung tissue but also amplifies the inflammatory response. It promotes macrophage transformation into a pro-inflammatory phenotype (M1-type), activates inflammatory vesicles and cellular pyroptosis, and triggers extensive cytokine release, further intensifying tissue damage [12-15]. Excessive NET deposition can also obstruct small airways, restricting airflow and further compromising the lungs' air-blood barrier function [16, 17]. Therefore, understanding NETs' mechanism of ac-

* Corresponding author.
E-mail addresses: doctorzjz@126.com (J. Zhang); dengbotjmu@126.com (B. Deng); 249880441@qq.com (Z. Tan)
Δ These authors contributed equally to this work.

https://doi.org/10.1016/S1875-5364(25)60874-0

tion in septic ALI and methods for removing excessive NETs is crucial for developing novel therapeutic approaches.

Traditional Chinese medicine (TCM) has demonstrated significant clinical efficacy and exhibits particular suitability for treating complex organ damage associated with sepsis through its multi-target and multi-pathway therapeutic benefits [18–20]. Taohe Chengqi decoction (THCQD), a classic formula derived from the *Treatise on Febrile Diseases* (*ShangHanLun*) [21], possesses properties that activate blood circulation, remove blood stasis, clear heat, and promote diarrhea. THCQD is effective in treating various diseases characterized by blood stasis. The formula comprises *Taoren* (Persicae Semen), *Dahuang* (Rhei Radix Et Rhizoma), *Guizhi* (Cinnamomi Ramulus), *Mangxiao* (mirabilite, sulfonitro-mineral mirabilite group), and *Gancao* (Glycyrrhizae Radix) [22]. These components work synergistically to enhance blood circulation while reducing inflammatory symptoms. THCQD achieves its therapeutic effects through multiple crucial signaling pathways and molecular targets. In treating sepsis-induced cardiac dysfunction, THCQD exhibits distinctive anti-ferroptosis properties essential for cardiac function restoration. Research indicates that THCQD may inhibit ferroptosis by activating the Nrf2 signaling pathway, providing anti-oxidant protection to the heart [21]. Furthermore, THCQD effectively improved metabolism-associated fatty liver by enhancing branched-chain amino acid catabolism in skeletal muscle of type 2 diabetes mellitus patients [22]. THCQD demonstrates significant anti-renal fibrosis effects by suppressing inflammatory responses, decreasing extracellular matrix (ECM) deposition, and reversing epithelial-mesenchymal transition (EMT) through the PI3K/protein kinase B (AKT)/mTOR and HIF-1α/VEGF signaling pathways [23]. THCQD has shown notable effectiveness in modulating inflammatory response and immunomodulation in sepsis-inducedALI. Molecular docking analyses revealed interactions between THCQD's active ingredients and key genes, including *MAPK14*, *MAPK3*, *MMP9*, *STAT3*, *LYN*, *AKT1*, *PTPN11*, and *HSP90AA1* [24]. Of particular significance is glycyrrhizic acid, an active component of licorice in THCQD, which effectively reduces sepsis-induced acute respiratory distress syndrome (ARDS) by inhibiting the HMGB1/TLR9 pathway and NET formation [25]. This study investigates THCQD's mechanism in ameliorating ALI and its relationship with NETs in sepsis patients, aiming to provide novel perspectives for clinical treatment and intervention.

2. Material and methods

2.1. Chemical and reagents

Iscove's modified Dulbecco's medium (IMDM, BL312A) was obtained from BioSharp (Hefei, China), while fetal bovine serum (FBS, C04001-500) was acquired from VivaCell (Shanghai, China). HL-60 cells were sourced from Pricella (Wuhan, China). Primary antibodies, including anti-histone H3 (ab281584) and anti-myeloperoxidase (ab208670), were acquired from Abcam (Cambridge, MA, USA), while anti-PADI4 (DF6685) and anti-neutrophil elastase (AF0010) were purchased from Affinity Biosciences (Santa Clara, CA, USA). An HRP-conjugated anti-rabbit IgG secondary antibody was obtained from Cell Signaling Technology (Danvers, MA, USA). Anti-F4/80 rabbit pAb (GB113373-100) and anti-Ly6g rabbit pAb (GB11229-100) were acquired from Solarbio (Solarbio, China). CXCR2 (20634-1-AP) and CXCL2 (26791-1-AP) were obtained from Proteintech Group, Inc. (Wuhan, China). Zombie Aqua™ Fixable Viability Kit (423101), APC/Cyanine7 anti-mouse/human cluster of differentiation 11b (CD11b) (101226), PE anti-mouse F4/80 (123110), fluorescein isothiocyanate (FITC) anti-mouse CD45 (103108), and Brilliant Violet 421M anti-mouse Ly-6G (127627) were acquired from BioLegend (San Diego, CA, USA). Collagenase type I and DNAase I were obtained from Worthington (Lakewood, NJ, USA) and Roche (Basel, Switzerland), respectively. Mouse cith3-11D3, mouse MPO-DNA, mouse interleukin-6 (IL-6), mouse tumor necrosis factor α (TNF-α), mouse IL-1β, human MPO-DNA, human cith3-11D3 were measured using enzyme-linked immunosorbent assay (ELISA) kits (Jiangsu Meimian Industrial Co., Ltd., China). Overexpression of peptidyl arginine deiminase 4 (PAD4) lentivirus was acquired from Genechem (Shanghai, China). Lipopolysaccharide (LPS), dexamethasone, and hyaluronidase H3884 were obtained from Sigma-Aldrich (St. Louis, MO, USA), while GSK484(S780) was procured from Selleck Chemicals (Houston, TX, USA). The THCQD formula, comprising *Taoren* (Batch No.: HX23G01), *Mangxiao* (Batch No.: HX22A01), *Dahuang* (Batch No.: HX23K01), *Guizhi* (Batch No.: HX23G01), and *Gancao* (Batch No.: HX23G01) were supplied by Guangdong Daxiang Traditional Chinese Medicine Pharmaceutical Co., Ltd.

2.2. Preparation and HPLC-Q-Exactive-MS Characterization of THCQD Extract

The THCQD extract was prepared according to our previously published protocol [21]: the herbs were soaked in pure water, decocted, and the resulting aqueous extract was filtered, concentrated, and lyophilized to yield a powder stored at –20 °C. Chemical characterization of the lyophilized powder by our established UHPLC-MS/MS method identified 72 constituents, whose details are provided in our published study [21].

2.3. Animals

Male C57/BL6 mice (18–20 g) were obtained from Guangzhou Ruige Biotechnology Co., Ltd. (Guangzhou, China). Forty C57/BL6 mice underwent a one-week acclimatization and feeding period. Following this adaptation phase, the mice were randomly assigned to the following groups: a sham surgery group, a cecum ligation group, a low-dose THCQD administration group (2 g·kg^{-1}, THCQD-L), a high-dose THCQD administration group (4 g·kg^{-1}, THCQD-H), and a positive control group receiving dexamethasone (1 mg·kg^{-1}, Dex) by gavage once daily for one week in each group. The model group, low-dose THCQD administration group, high-dose THCQD administration group, and Dex (as a positive control) group underwent ALI induction through the cecum ligation and puncture (CLP) method to establish the mouse sepsis model. (Animal experimentation ethics number: GY2024-282).

2.4. CLP

In the experimental protocol, mice underwent a 12-hour fasting period prior to weighing. Anesthesia was administered *via* intraperitoneal injection of sodium pentobarbital at a dosage of 50 mg·kg^{-1}, with dose adjustments according to each mouse's body weight. The mice were placed in a supine position, their limbs were secured, and abdominal hair was removed using depilatory cream. Sterilization was conducted using 75% ethanol-soaked cotton balls, followed by povidone iodine application. Surgical instruments were sterilized through ethanol immersion. A 1 cm incision was created along the lower abdominal midline to access the cecum. The appropriate ligation site on the cecum was identified based on existing literature. Following ligation, the cecum was punctured with a 20-gauge needle to enable fecal drainage through the puncture hole. The ligated cecum was carefully returned to the abdominal cavity, and the peritoneum and skin were sutured [15, 21, 26, 27]. Post-surgery, the mice were placed on a temperature-controlled heating pad to maintain body temperature and prevent hypothermic shock and potential mortality.

2.5. Histopathologic examination

Mouse lungs were irrigated in phosphate-buffered saline (PBS) before being aseptically excised and fixed in 4% paraformaldehyde (PFA). Following fixation, the samples underwent sequential processing including graded ethanol dehydration, xylene vitrification, and paraffin embedding. The paraffin-embedded lungs were sectioned to a thickness of 5 μm using a sectioning machine. Sections were heated at 60 °C for 30 min, deparaffinized, rinsed with double-distilled water, and stained with hematoxylin-eosin (H&E). Following staining, the slides underwent dehydration with graded alcohol, clearing, and mounting with neutral resin. The mounted sections were allowed to dry completely. After drying, the sections were examined and photographed using inverted light microscopy, and the images were documented for subsequent analysis. Lung injury scores were determined based on lung tissue edema, hemorrhage, inflammatory cell infiltration, and alveolar wall thickness [28].

2.6. Western blotting assay

HL-60 cells were harvested and lysed with a lysis solution. Cells were lysed by centrifugation (P0013B, Beyotime), and the supernatant was collected for protein concentration determination using a BCA kit (23225, Thermo Fischer Scientific). Western blotting of proteins onto polyvinylidene difluoride (PVDF) membranes (IPVH00010, Millipore) was blocked for 60 minutes, followed by primary antibody incubation at 4 °C for 13 h, then secondary antibody at room temperature for 90 min. Protein bands were visualized using the ECL system (Tanon4600). Protein band intensity analysis was performed using ImageJ software.

2.7. Flow cytometry analysis of single-cell suspensions of lungs

The mouse lung tissues were perfused with ice-cold PBS until blood was completely removed. Subsequently, the lung tissue was minced into small pieces and digested in a mixture of collagenase type I and DNase I on a shaking table at 37 °C for 40 min. After digestion, the tissue samples were incubated with anti-mouse CD45-FITC, CD3-APC, CD11b-APC, F4/80-PE, and Ly6G-BV421 in PBS. The immune cell populations were then quantitatively analyzed using flow cytometry.

2.8. Immunofluorescence

Lung histopathology sections were permeabilized in PBS containing 0.5% Triton X-100 for 10 min and blocked in 5% goat serum for 60 min. Subsequently, the sections were incubated with specified primary antibodies at 4 °C for 12 h. The sections were then washed twice in PBS and incubated at 26 °C for 60 min with the corresponding secondary antibody. Cell nuclei were counterstained with 4',6-diamidino-2-phenylindole (DAPI) for 10 min. The samples were examined using fluorescence microscopy to detect fluorescent signals from labeled antibodies for visualization of target cells and subcellular structures. DAPI staining facilitated the identification and localization of nuclei in tissue sections.

2.9. Real-time polymerase chain reaction (PCR)

Total ribonucleic acid (RNA) was extracted using TRIzol® reagent (Invitrogen Life Technologies; Thermo Fisher Scientific, USA). Reverse transcription was performed using the Evo M-MLV Reagent Premix for Reverse Transcription. For real-time RNA quantification, the SYBR Green Premix Pro Taq HS quantitative PCR (qPCR) Kit was employed. Primer sequences for the qPCR were obtained from Sangon Biotechnology Co. The primer sequences were designed as follows: Human: IL-6: 5'-CACTCACCTCTTCAGAACGAAT, 3'-GCTGCTTTCACACATGTTACTC; TNF-α: 5'-CCAGGGACCTCTCTCTAATCA, 3'-TCAGCTTGAGGGTTTGCTAC; IL-1β: 5'-GGACAGGATATGGAGCAACAA, 3'-CCCAAGGCCACAGGTATTT;PAD4: 5'-CCCTCCAGCCAAGAAGAAAT, 3'-AGTCTTGGGTCCGTAGTATGA. Mouse: IL-6: 5'-TCCATCCAGTTGCCTTCTTG, 3'-GGTCTGTTGGGAGTGGTATC; TNF-α: 5'-ACGGCATGGATCTCAAAGAC, 3'-CGGACTCCGCAAAGTCTAAG; IL-1β: 5'-AGCTCTCCACCTCAATGGAC, 3'-GACAGGCTTGTGCTCTGCTT; CXCR2: 5'-CTGTCTGGGCTGCATCTAAA, 3'-GTAGCAGAACACTGCTGTAGAA; CXCL2: 5'-TCAAGAACATCCAGAGCTTGAG, 3'-CTTCAGGGTCAAGGCAAACT; 18S: 5'-TGGTTGCAAAGCTGAAACTTAAAG, 3'-AGTCAAATTAAGCCGCAGGC.

2.10. Cell culture

HL-60 cells were cultured in IMDM supplemented with 20% fetal bovine serum. The cells were induced to differentiate into neutrophils over 5 d using a medium containing 1.3% dimethyl sulfoxide (DMSO). THCQD at concentrations of 50, 100, and 200 $\mu g \cdot mL^{-1}$ was administered for 12 h. NETs were induced by treating cells with LPS at 200 $ng \cdot mL^{-1}$ or phorbol 12-myristate 13-acetate (PMA) at 300 $ng \cdot mL^{-1}$ for 3 h.

2.11. Giemsa staining

Cell smears were prepared following conventional methods. After the cells dried, they were positioned flat on the staining rack. Subsequently, 200–400 μL of Giemsa stain solution was rapidly applied to cover the cells. Following 90–120 sec of staining, 1–2 times the volume of Giemsa buffer solution was added, and the slides were gently agitated to ensure thorough mixing. The staining continued for an additional 5–8 min. The cells were then slowly rinsed with tap water from one end of the slide for 30 sec and air-dried. Finally, the slides underwent a second 30-second rinse with tap water before being dried for microscopic examination.

2.12. Sytox green staining

DMSO-induced HL-60 cells were incubated with 10 $nmol \cdot L^{-1}$ Sytox green for 15 min in a 37 °C incubator. Subsequently,1 × Hoechst 33342 was added, followed by an additional 15-min incubation at 37 °C. After discarding the staining solution, the cells were gently washed twice with PBS or culture medium in preparation for fluorescence detection. The slides were then slowly rinsed with tap water for 30 sec and air-dried before microscopic examination.

2.13. Extraction of primary neutrophils from mouse bone marrow

Mice were euthanized by cervical dislocation and sterilized using 75% ethanol either by spraying or immersion. An incision was made at the mouse's ankle with a scalpel, followed by a longitudinal cut along the leg bone. The leg skin was retracted, and muscles near the thigh root were removed. The entire leg was excised at the hip joint using a scalpel, the Achilles tendon was severed, and major muscles surrounding the tibia were removed. The femoral muscles were removed using scissors, the knee joint soft tissue was excised to access the femur, and the fibula and surrounding muscles were cut to expose the intact tibia.

The femoral and tibial epiphyses were resected, and bone marrow was extracted using a 1 ml syringe containing 1640 medium with 10% FBS. The bone marrow was rinsed into a petri dish using approximately 2–3 mL per bone, carefully avoiding medium reflux to prevent contamination. Neutrophils with greater than 80% purity were isolated from the bone marrow cell sus-

pension using the Mouse Bone Marrow Neutrophil Isolate Kit (Solebo).

2.14. ELISA

Cell culture supernatant was collected in sterile tubes and centrifuged at 2–8 °C for 20 min. The supernatant was collected and added to 96-well plates from the kit along with prepared standards. The mixture was incubated at 37 °C for 30 min, followed by three wash cycles and the addition of an enzyme labeling reagent. After another 30-min incubation at 37 °C andthree wash cycles, color developers A and B were added. The reaction proceeded for 10 min at 37 °C in darkness before adding the termination solution. Using blank wells for zero calibration, absorption was measured at 450 nm, and absorbance values were calculated.

2.15. Molecular docking

Molecular docking analyses were performed using Autodock Vina software to investigate the conjugation interactions between PAD4 and THCQD's active ingredients. The PAD4 spatial structure (PDB ID: 3B1T) served as the target protein. The molecular docking simulations were preceded by removing water molecules and ligands from the original spatial structure to generate refined PAD4 molecular docking simulation proteins. Following target protein preparation, molecular docking simulations were conducted, and optimal conformations were carefully selected for subsequent analysis.

2.16. Lentivirus transfection

The experiment was conducted following established protocols. Initially, puromycin working concentration screening was performed. HL-60 cells were inoculated in a 24-well plate to achieve 80% cell density per well after 24 h. Various puromycin concentrations were introduced to the wells. Subsequently, HL-60 cells were cultured in six-well plates (2×10^5 cells/well), and lentivirus was introduced the following day at a 40-fold multiplicity of infection (MOI). After 16 h of incubation, the medium was replaced and changed again the next day until 72 h. Infection efficiency was monitored using a fluorescence microscope. When infection density reached 70%–80%, 5 μg·mL^{-1} puromycin was administered for 72 h cell screening. After the complete elimination of control cells (non-lentivirus infected), the remaining lentivirus-transferred cells were considered successfully infected. The HL-60 cells were then maintained with 1 μg·mL^{-1} puromycin to establish stable infection. Some cells were collected for Western blotting verification, while the majority were cultured for additional experiments, including qPCR, Sytox green, and cellular immunofluorescence assay.

2.17. Statistical analysis

Statistical analysis was performed using GraphPad Prism 9 software, with results expressed as mean ± standard deviation (SD). The *t*-test was employed for two-group comparisons. Multiple comparisons utilized Tukey's post-hoc test and one-way ANOVA. Statistical significance was established at *P*-values below 0.05. $^{*}P < 0.05$; $^{**}P < 0.01$.

3. Results

3.1. THCQD improved survival rate and alleviated lung injury in a CLP-induced ALI mouse model

The study first examined THCQD's protective effects against

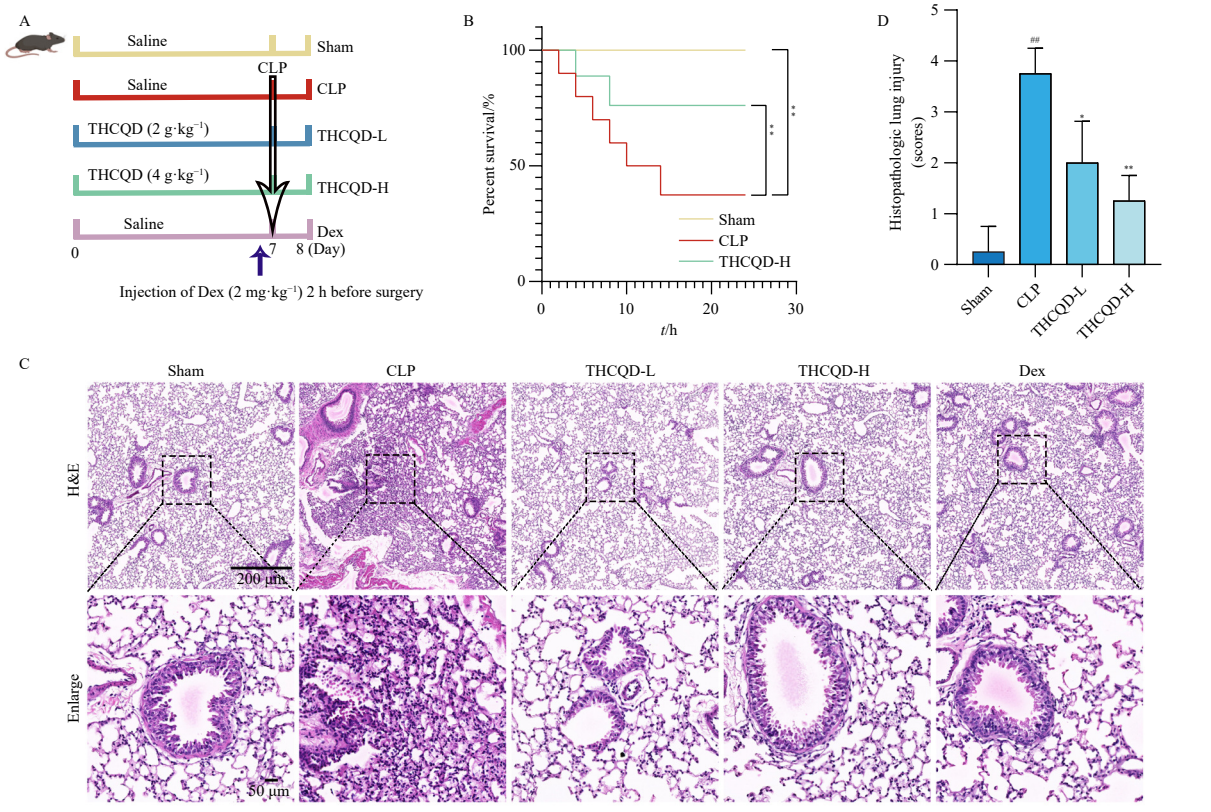

Fig. 1 THCQD improved survival rate and alleviated lung injury in a CLP-induced ALI mouse model. (A) Mice were gavaged with Dex (2 mg·kg^{-1}) and THCQD (2 and 4 g·kg^{-1}). (B) Kaplan-Meier survival analysis of different groups of mice, $n = 10$ per group. (C) Representative sections of H&E-stained lung tissues. Scale bar represents 200 μm. Representative H&E-stained sections of mouse lung tissue. Scale bar represents 50 μm. (D) Lung injury score ($n = 4$). Data are presented as the mean accompanied by the standard deviation (mean ± SD). $^{\#}P < 0.05$, $^{\#\#}P < 0.01$ *vs* sham; $^{*}P < 0.05$, $^{**}P < 0.01$ *vs* CLP.

CLP-induced ALI *in vivo*. Following a one-week acclimatization period, mice received THCQD through gavage for one week. After 12-h fasting, the mice were allocated into CLP, THCQD-L, THCQD-H, and Dex groups. The ALI model was established through CLP, and mice were sacrificed after 24 h. Fig. 1A illustrates the experimental methodology. Mouse mortality was monitored at specific intervals to assess THCQD's effect. The results demonstrated that THCQD treatment significantly enhanced survival rates compared to the CLP-only group (Fig. 1B). The CLP group displayed more severe lung tissue damage than the control group, characterized by alveolar wall thickening and inflammatory cell infiltration (Fig. 1C). THCQD and Dex administration markedly reduced lung pathological lesions. H&E staining revealed that THCQD pretreatment significantly decreased lung injury, as evidenced by the lung injury score (Fig. 1D). These findings indicated THCQD's effectiveness in alleviating CLP-induced ALI in mice.

3.2. THCQD decreased macrophage infiltration and inflammation

Previous studies have demonstrated that C57/BL6 mice subjected to CLP for 24 hours develop severe acute lung inflammation, characterized by increased macrophage infiltration [29]. Our findings revealed a significant decrease in macrophage numbers in the THCQD treatment group compared to the CLP group, as demonstrated through immunofluorescence and flow cytometry analyses (Figs. 2A–2E). The study also examined serum levels of key inflammatory cytokines, including IL-1β, IL-6, and TNF-α. These cytokines showed elevation in the CLP group, while THCQD treatment effectively lowered their concentrations relative to the CLP group (Figs. 2F–2H). Moreover, the messenger RNA (mRNA) expression of pro-inflammatory cytokines (IL-1β, IL-6, and TNF-α) exhibited significant elevation in the CLP group compared to controls, whereas THCQD administration reduced their relative expression (Figs. 2I–2K). Western blotting analysis confirmed that IL-1β expression in CLP mice cardiac tissue decreased significantly following THCQD treatment (Figs. 2L–2M). These results indicate that THCQD effectively suppressed macrophage infiltration and inflammation *in vivo*.

3.3. THCQD decreased neutrophil infiltration and recruitment in a CLP-induced ALI mouse model

Research has established that neutrophils migrate into the lungs and execute various pro-inflammatory functions, which are essential for the initiation, progression, and resolution of complex inflammatory processes [30]. This study investigated THCQD's effects on neutrophil infiltration and subsequent neutrophil-mediated immunological responses. Neutrophil recruitment was assessed using flow cytometry and immunostaining techniques. IF analysis demonstrated that CLP-operated mice exhibited significantly elevated Ly6G expression in lung tissues, while THCQD-treated groups showed markedly reduced expression (Figs. 3A–3B). Flow cytometric analysis of lung single-cell suspensions from CLP-treated mice confirmed this pattern, revealing decreased neutrophil accumulation in THCQD-administered groups compared to the CLP group (Figs. 3C–3E). Furthermore, CXCL2/CXCR2 signaling, which functions as a pro-inflammatory cytokine system with chemotactic effects on neutrophils and activated monocytes, is expressed at inflammatory sites and regulates neutrophil infiltration and recruitment. CXCR2 and CXCL2 represent chemokines that influence macrophages and neutrophils and are fundamental to inflammation. Immunofluorescence analysis of lung tissues revealed reduced CXCR2 and CXCL2 expression in the THCQD-administered group compared to the CLP group (Figs. 3F–3I). These findings demonstrate that THCQD inhibited neutrophil infiltration and recruitment while reducing CXCR2 and CXCL2 expression.

3.4. THCQD inhibited NET formation in vivo

During sepsis-induced ALI, neutrophils migrate into the alveolar spaces, where NET formation occurs, resulting inNETosis [31]. To investigate the effect of THCQD on NET formation in mouse serum, we evaluated the levels of MPO/DNA complexes and citrullinated histone H3 (citHis3)--specific biomolecules associated with NETs--using ELISA. The results demonstrated that CLP significantly elevated MPO/DNA complexes and citHis3 levels, while THCQD treatment effectively reduced these elevations (Figs. 4A–4B). Furthermore, immunofluorescence staining for MPO and PAD4 in lung tissues corroborated these findings, indicating that THCQD may inhibit NET formation (Figs. 4C–4D). Western blotting analysis revealed a significant reduction in the relative expression of NETs-related proteins, including MPO, PAD4, NE, and citHis3, in mice treated with THCQD compared to the CLP group (Figs. 4E–4H). These findings collectively demonstrated that THCQD inhibited NET formation in CLP-induced ALI.

3.5. THCQD inhibited LPS-induced NET formation in neutrophil-like cells in vitro

Fig. 5A demonstrated Giemsa staining results of HL-60 cells induced by DMSO for 5 d, indicating that more than 80% of the nuclei exhibited lobulation. Sytox Green staining revealed enhanced free DNA presence with filamentous characteristics in the LPS model group (Fig. 5B). Analysis of MPO/DNA complexes and citHis3 in the cell culture supernatant revealed a significant increase in the LPS-treated group and subsequent reduction in the THCQD-treated group (Figs. 5C–5D). Western blotting analysis demonstrated a substantial decrease in NET-related protein levels in the THCQD-treated group compared to the LPS model group (Figs. 5E–5I). Immunofluorescence staining indicated elevated PAD4 fluorescence intensity in the LPS model group, which diminished in the THCQD-treated group (Fig. 5J). The mRNA levels of inflammatory cytokines *IL-1β*, *IL-6,* and *TNF-α* exhibited significant elevation after LPS stimulation and decreased following THCQD administration (Figs. 5K–5M).

3.6. THCQD inhibited LPS-induced NET formation and PAD4 activity in vitro

The study employed LPS for modeling and incorporated DNase Ⅰ, an established positive drug for NETs [32–34], to evaluate its efficacy compared to THCQD. Results demonstrated that THCQD reduced the expression of NET-associated proteins, including MPO, PAD4, NE, and citHis3 (Figs. 6A–6E). Furthermore, utilizing GSK484 (10 μmol·L^{-1}), a specific PAD4 inhibitor [35, 36], protein immunoblotting analysis revealed that THCQD significantly suppressed PAD4 production. Cellularimmunofluorescence staining confirmed this finding, showing markedly reduced PAD4 fluorescence intensity following THCQD administration (Figs. 6F–6H).

3.7. THCQD inhibited PMA-induced NET formation in neutrophil-like cells in vitro

The study also utilized PMA, an established cell model for NET formation [37–40], as a comparative model to LPS. Western blotting analysis revealed a substantial reduction in NET-related proteins in the THCQD-treated group compared to the PMA model group (Figs. 7A–7E). Sytox Green staining demonstrated elevated levels of free DNA in the PMA model group (Fig. 7F). Immunofluorescence staining indicated higher PAD4 and citHis3 fluorescence intensities in the PMA model group, with citHis3 exhibiting a distinct reticular structure. THCQD treatment significantly decreased both the fluorescence intensity and reticular structure formation (Figs. 7G–7H).

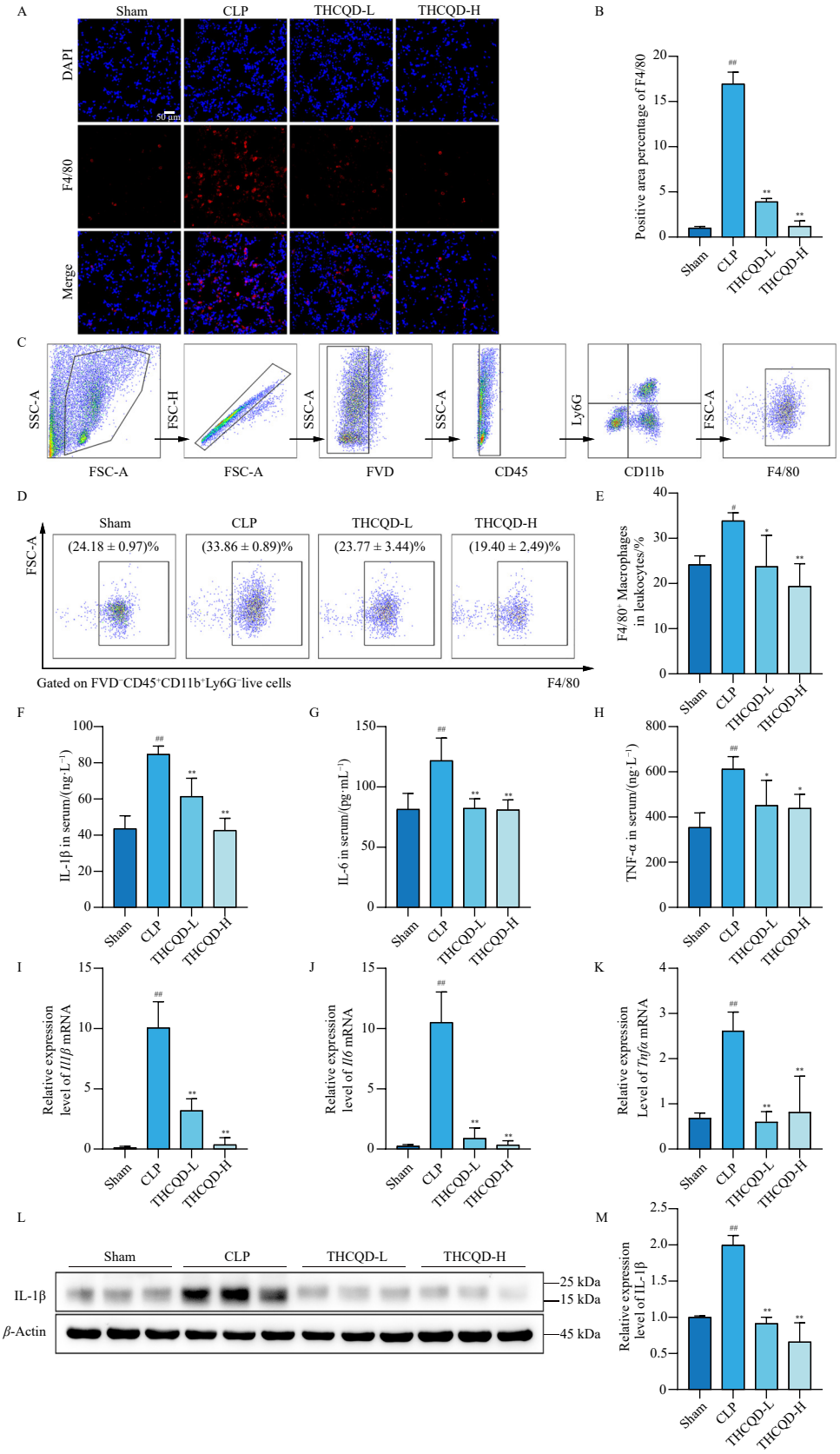

Fig. 2 THCQD decreased macrophage infiltration and inflammation. (A) Representative immunofluorescence images of lung tissue sections stained for the macrophage marker F4/80 (green) and counterstained with DAPI for nuclei (blue). Scale bar, 50 μm. (B) Quantification of F4/80-positive cells in lung sections (n = 3). (C) Gating strategy used for flow cytometric identification of macrophage populations from lung tissue. (D) Quantification of macrophages as a proportion of total leukocytes by flow cytometry in saline control, CLP model, low-dose THCQD, and high-dose THCQD groups (n = 4). (E) Representative flow cytometry plots of lung macrophage populations. (F–H) Serum concentrations of IL-1β (n = 6), IL-6 (n = 6), and TNF-α (n = 4) measured by ELISA. (I–K) Relative mRNA expression levels of IL-1β, IL-6, and TNF-α in lung tissue, determined by quantitative PCR (n = 3). (L–M) Western blotting analysis and densitometric quantification of IL-1β protein expression in lung tissue samples (n = 3). Data are presented as the mean accompanied by the standard deviation (mean ± SD). $^{\#}P < 0.05$, $^{\#\#}P < 0.01$ *vs* sham; $^{*}P < 0.05$, $^{**}P < 0.01$ *vs* CLP.

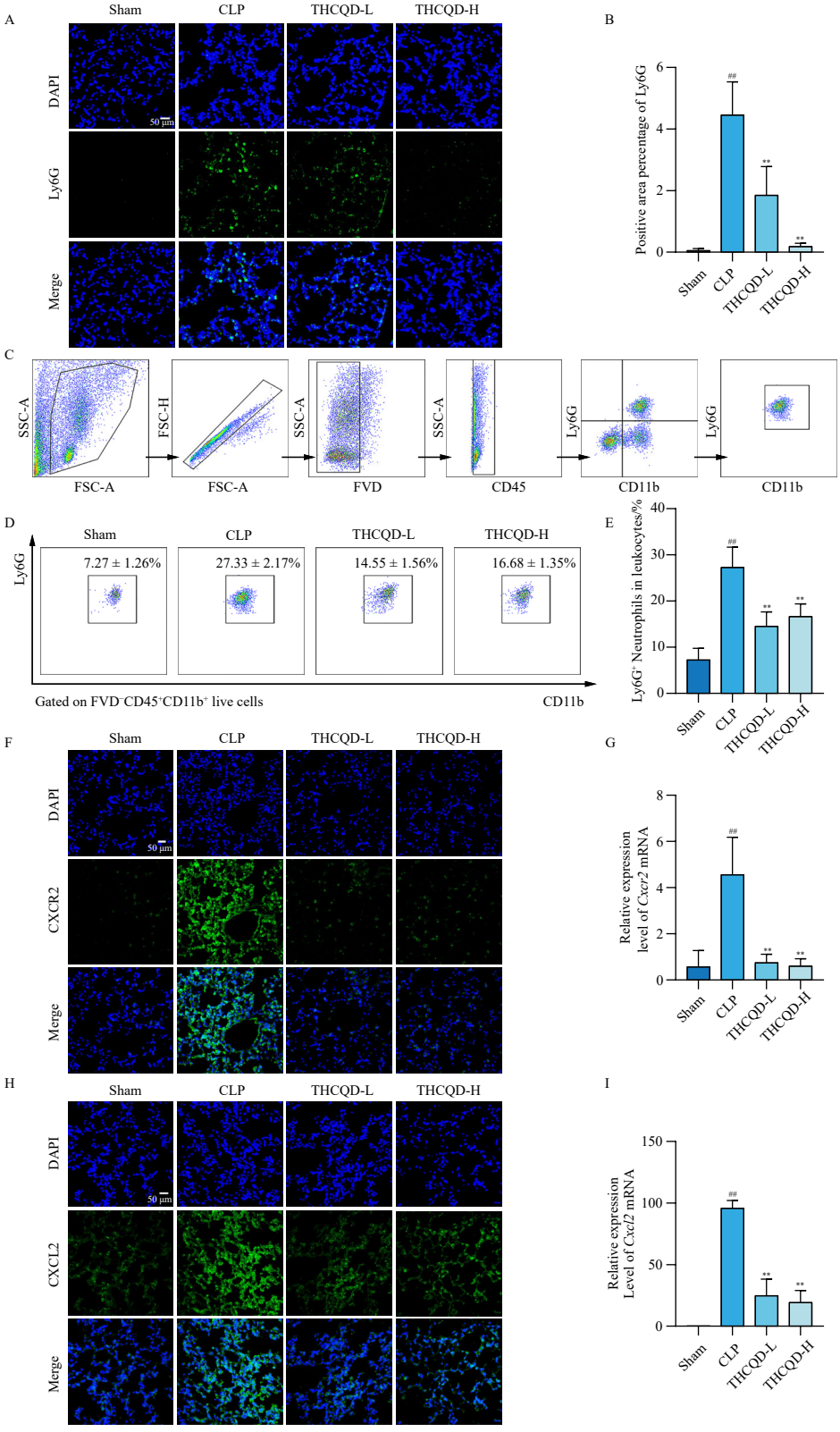

Fig. 3 THCQD decreased neutrophil infiltration and recruitment in a CLP-induced ALI mouse model. (A) Representative immunofluorescence images of lung tissue stained for Ly6G (green), a neutrophil marker, with DAPI (blue) for nuclear counterstaining. Scale bar: 50 μm. (B) Quantification of Ly6G-positive cells in lung tissue (n =3). (C) Gating strategy used for flow cytometric identification of neutrophil populations isolated from lung tissue in each group. (D) Proportional analysis of neutrophils among total leukocytes in the saline control, CLP model, low-dose THCQD, and high-dose THCQD groups, determined by flow cytometry (n = 4). (E) Representative flow cytometry plots illustrating neutrophil populations across treatment groups. (F) Immunofluorescence staining of lung sections for CXCR2 (green), with DAPI (blue) nuclear counterstaining. Scale bar, 50 μm. (G) Relative mRNA expression levels of *CXCR2* in lung tissue, detected by qPCR (n = 3). (H) Representative immunofluorescence images of lung tissue stained for CXCL2 (green), a key neutrophil chemoattractant, with DAPI (blue). Scale bar: 50 μm. (I) Relative mRNA expression of *CXCL2* in lung tissue was detected by qPCR (n = 3). Data are presented as the mean accompanied by the standard deviation (mean ± SD). $^{\#}P < 0.05$, $^{\#\#}P < 0.01$ *vs* sham; $^{*}P < 0.05$, $^{**}P < 0.01$ *vs* CLP.

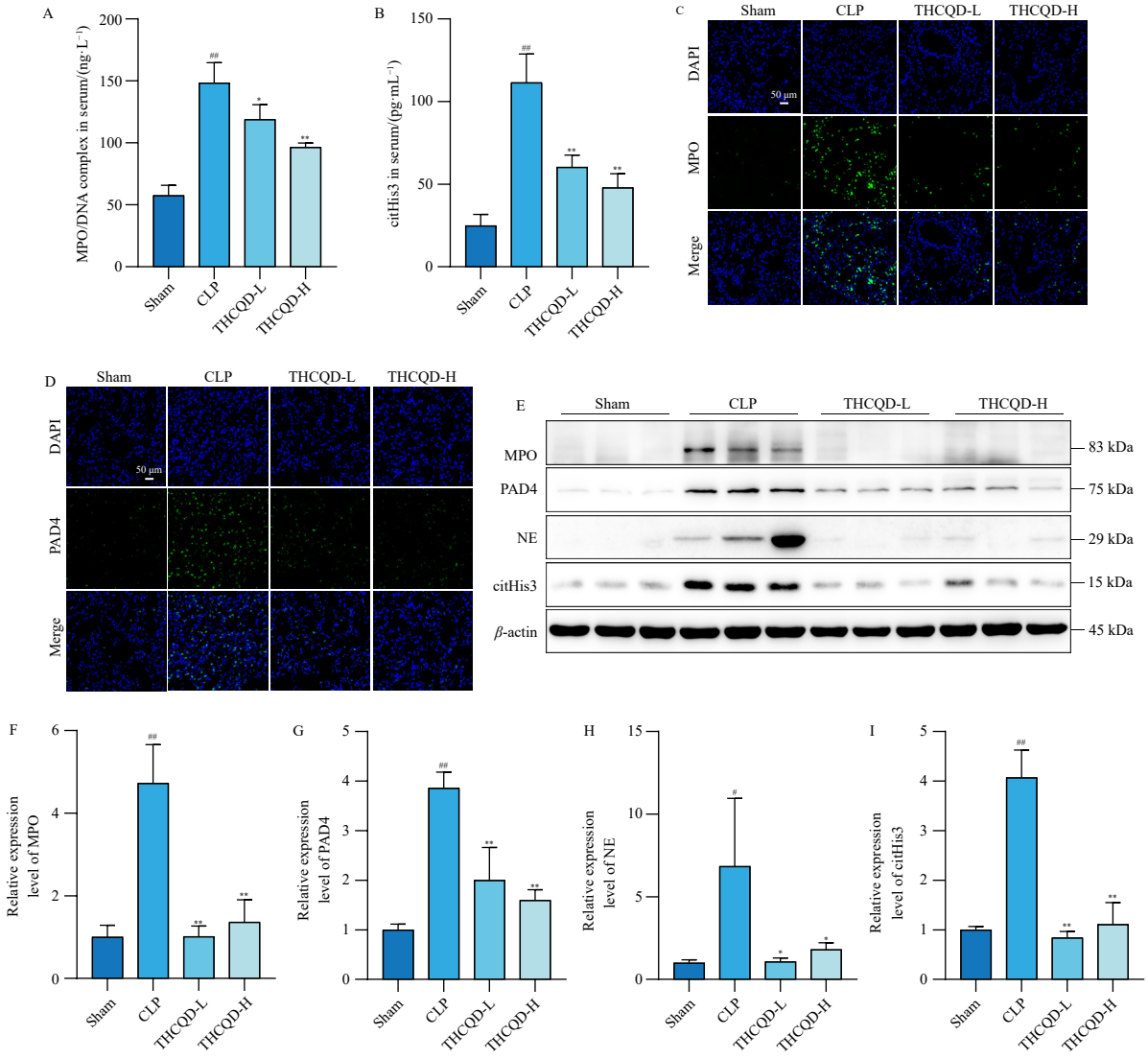

Fig. 4 THCQD inhibited NET formation *in vivo*. (A–B) Quantification of the serum levels of MPO/DNA complexes (n = 3) and citHis3 (n = 3) by ELISA. (C–D) Representative immunofluorescence images of lung tissues stained for MPO and PAD4, with DAPI (blue) nuclear counterstaining. Scale bar, 50 μm. (E) Western blotting analysis of NET-associated proteins, includin MPO, citH3, and PAD4, in lung tissue samples. (F–I) Quantification of Western blotting bands for NET-associated markers (n = 3). Data are presented as the mean accompanied by the standard deviation (mean ± SD). $^{\#}P < 0.05$, $^{\#\#}P < 0.01$ *vs* sham; $^{*}P < 0.05$, $^{**}P < 0.01$ *vs* CLP.

3.8. THCQD inhibited PMA-induced NET formation in mouse bone marrow-derived neutrophils in vitro

Primary neutrophils were isolated from mouse bone marrow and subjected to PMA to evaluate NET formation. Giemsa staining revealed lobulated nuclei in these cells, confirming their identity as primary neutrophils with a purity exceeding80% (Fig. 8A). Sytox Green staining indicated enhanced free DNA and reticulation in the PMA model group (Fig. 8B). Immunofluorescence staining demonstrated elevated PAD4 and citHis3 fluorescence intensities in the PMA model group, with citHis3 forming a distinct reticular structure. The THCQD-treated group exhibited decreased fluorescence intensity and less prominent reticular structure (Figs. 8C–8D).

3.9. THCQD can directly target PAD4

Previous research identified 72 compounds in the analysis of THCQD using the UHPLC-Q-Orbitrap HRMS approach (Fig. S1 and Table S1). The bioactive components included glycyrrhizin, licoricesaponin H, emodin-8-glucoside, pulmatin, rhein 8-glucoside, vitexin-2-*O*-rhamnoside, gancaonin E and lindleyin. Autodock Vina was employed to evaluate the association between PAD4 (PDB ID: 3B1T) and the active ingredients in THCQD. The analysis revealed significant binding energies for several compounds: glycyrrhizin showed −9.19 kcal·mol^{-1}, licoricesaponin H exhibited −9.03 kcal·mol^{-1}, emodin-8-glucoside demonstrated −8.02 kcal·mol^{-1}, pulmatin displayed −7.90 kcal·mol^{-1}, rhein 8-glucoside showed −7.89 kcal·mol^{-1}, vitexin-2-*O*-rhamnoside exhibited −7.83 kcal·mol^{-1}, gancaonin E showed −7.82 kcal·mol^{-1}, and lindleyin −7.80 kcal·mol^{-1} (Fig. 9). The molecular docking results indicated that the active ingredients in THCQD possess strong binding affinity for the PAD4 complex. Fig. 9 presented a three-dimensional binding model of the interaction between the active ingredients and PAD4 in THCQD.

3.10. Overexpression of PAD4 impeded the formation of NETs and partially restricted the inhibitory effect of THCQD on PAD4

As illustrated in Fig. 10A, lentiviral transduction did not affect neutrophil morphology, while Fig. 10B confirms successful overexpression of PAD4, with mRNA levels elevated approximately 40-fold compared to normal levels. To determine whether PAD4 mediates the inhibitory effects of THCQD on NET formation, we assessed NET production in PAD4-overexpressing neutrophils treated with THCQD using Sytox Green staining (Fig. 10C).

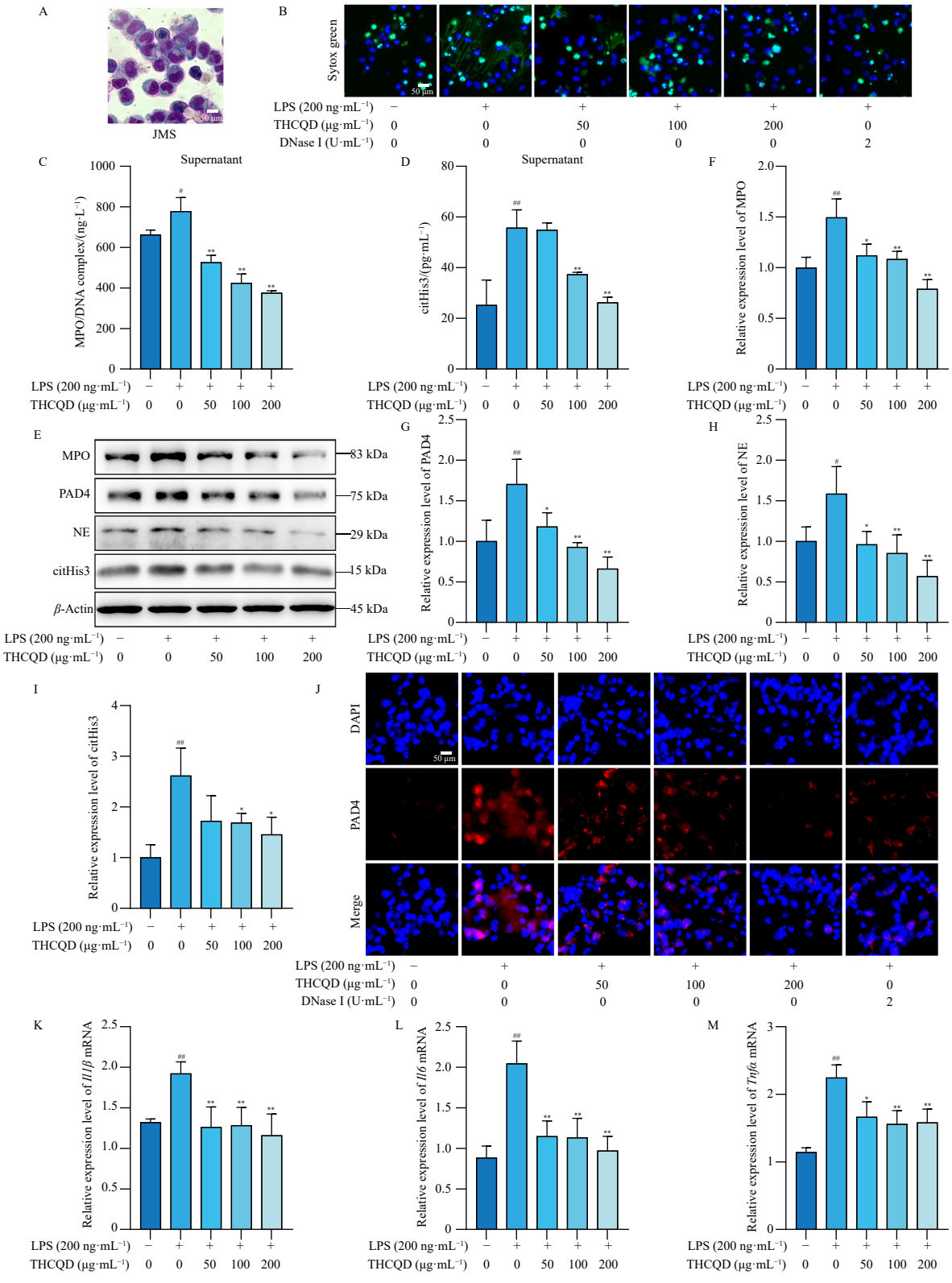

Fig. 5 THCQD inhibited LPS-induced NET formation in neutrophil-like cells *in vitro*. (A) Results of Giemsa staining. Scale bar, 50 μm. (B) Sytox green staining results. Scale bar, 50 μm. (C–D) Detection of MPO/DNA complex and citHis3 levels in cell supernatants by ELISA (n = 3). (E) Western blotting analysis of NET-associated proteins, including MPO, PAD4, NE, and citHis3. (F–I) Results of quantitative analysis of MPO, PAD4, NE, and citHis3 proteins (n = 3). (J) Characteristic immunofluorescence images showing intracellular PAD4 localization with DAPI nuclear counterstaining *in vitro*. Scale bar, 50 μm. (K–M) Relative mRNA expression levels of *IL-1β*, *IL-6*, and *TNF-α* in cells were measured by qPCR (n = 3). Data are presented as the mean accompanied by the standard deviation (mean ± SD). $^{\#}P < 0.05$, $^{\#\#}P < 0.01$ *vs* control; $^{*}P < 0.05$, $^{**}P < 0.01$ *vs* LPS.

The results revealed that the inhibitory effect of THCQD on NETs production was significantly reversed in the PAD4-overexpressing (PAD4-OE) group compared to the negative control (NC) group (Figs. 10D–10E). Immunofluorescence staining confirmed this effect visually (Fig. 10F). These findings indicated that THCQD reduced NET formation through PAD4 inhibition4.

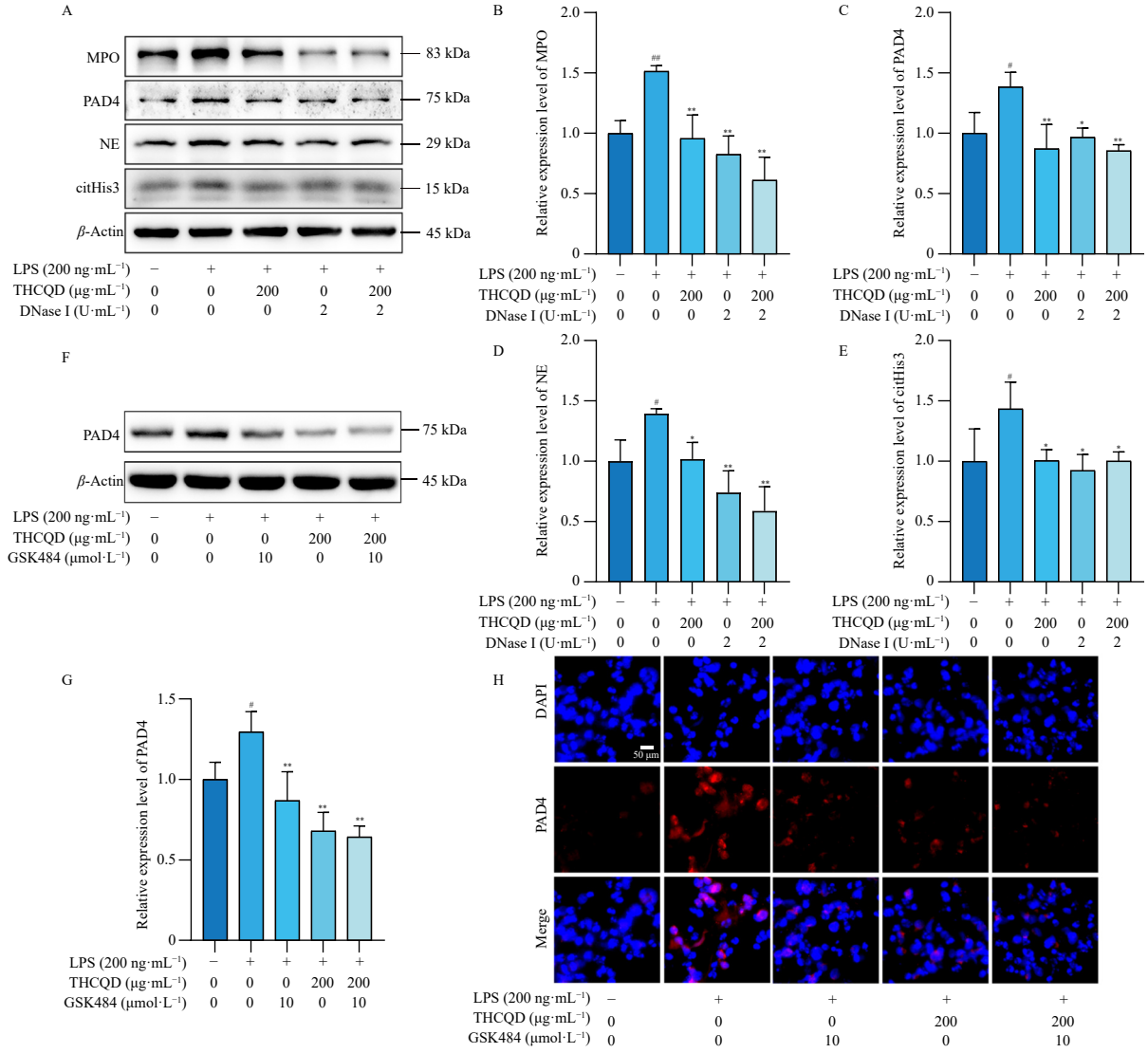

Fig. 6 THCQD inhibited LPS-induced NET formation and PAD4 activity *in vitro*. (A) Western blotting analysis of key NET-associated proteins, including MPO, PAD4, NE, and citHis3, in LPS-stimulated neutrophil-like cells. DNase Ⅰ (2 U·mL^{-1}) was used as a positive control. (B–E) Densitometric quantification of MPO, PAD4, NE, and citHis3 protein levels (n = 3). (F) Western blotting analysis of PAD4 expression following treatment with in cells with THCQD, with GSK484 (10 μmol·mL^{-1}) as a positive control. (G) Quantitative analysis of PAD4 expression (n = 3). (H) Representative immunofluorescence images showing localization *in vitro*, with nuclear counterstaining by DAPI. Scale bar, 50 μm. Data are presented as the mean accompanied by the standard deviation (mean ± SD). $^{\#}P < 0.05$, $^{\#\#}P < 0.01$ *vs* control; $^{*}P < 0.05$, $^{**}P < 0.01$ *vs* LPS.

4. Discussion

ALI is a pathological condition characterized by diffuse interstitial pulmonary edema resulting from damage to pulmonary microvascular endothelial cells and alveolar epithelial cells caused by various pathogenic factors [41–43]. Among the multiple factors contributing to ALI, sepsis remains the primary risk factor [44]. Despite significant advances in anti-infective therapy and organ function support in recent years, specific pharmacological interventions for sepsis-induced ALI remain limited [45]. Currently, the international treatment of sepsis primarily relies on hormonal drugs, which are associated with significant side effects. Furthermore, the exclusive use of antibiotics in sepsis treatment has shown suboptimal results, with most clinical interventions addressing symptoms rather than underlying causes [46]. Modern drug research trends toward multi-target drug development, and TCM offers extensive historical documentation and compound formulas. TCM's therapeutic mechanism operates through multiple targets and levels, with substantial experimental research confirming its efficacy in treating infections, inflammation, and related diseases [47–49]. This study demonstrates that the TCM formulation THCQD effectively ameliorates ALI induced by the CLP model, thereby extending survival time.

ALI progression involves significant infiltration of inflammatory cells, particularly neutrophils and macrophages, into pulmonary tissues [50]. Additionally, the enhanced release of inflammatory mediators and chemokines further compromises alveolar and capillary barrier integrity [51]. Our findings demonstrate that THCQD reduces IL-1β, IL-6, and TNF-α protein and mRNA levels in both mouse serum and lung tissue during ALI. Flow cytometry analysis of lung single-cell suspensions revealed that THCQD significantly inhibited inflammatory cell infiltration, including macrophages and neutrophils, correlating with improved histopathological findings. Immunofluorescence experiments confirm substantial reductions in macrophage and neutrophil expression, accompanied by decreased chemokine receptor levels following THCQD treatment.

Furthermore, our *in vitro* experiments investigated THCQD's effect on LPS-induced neutrophil-like NET formation. The results indicate that THCQD reduced NET levels in LPS-induced neutrophil-like cells and downregulated MPO, PAD4, NE, and citHis3 expression. Numerous studies have identified PMA as a well-established NET inducer [52, 53]. Our investigation extended to PMA-induced neutrophil-like NET formation. Primary neutrophils ex-

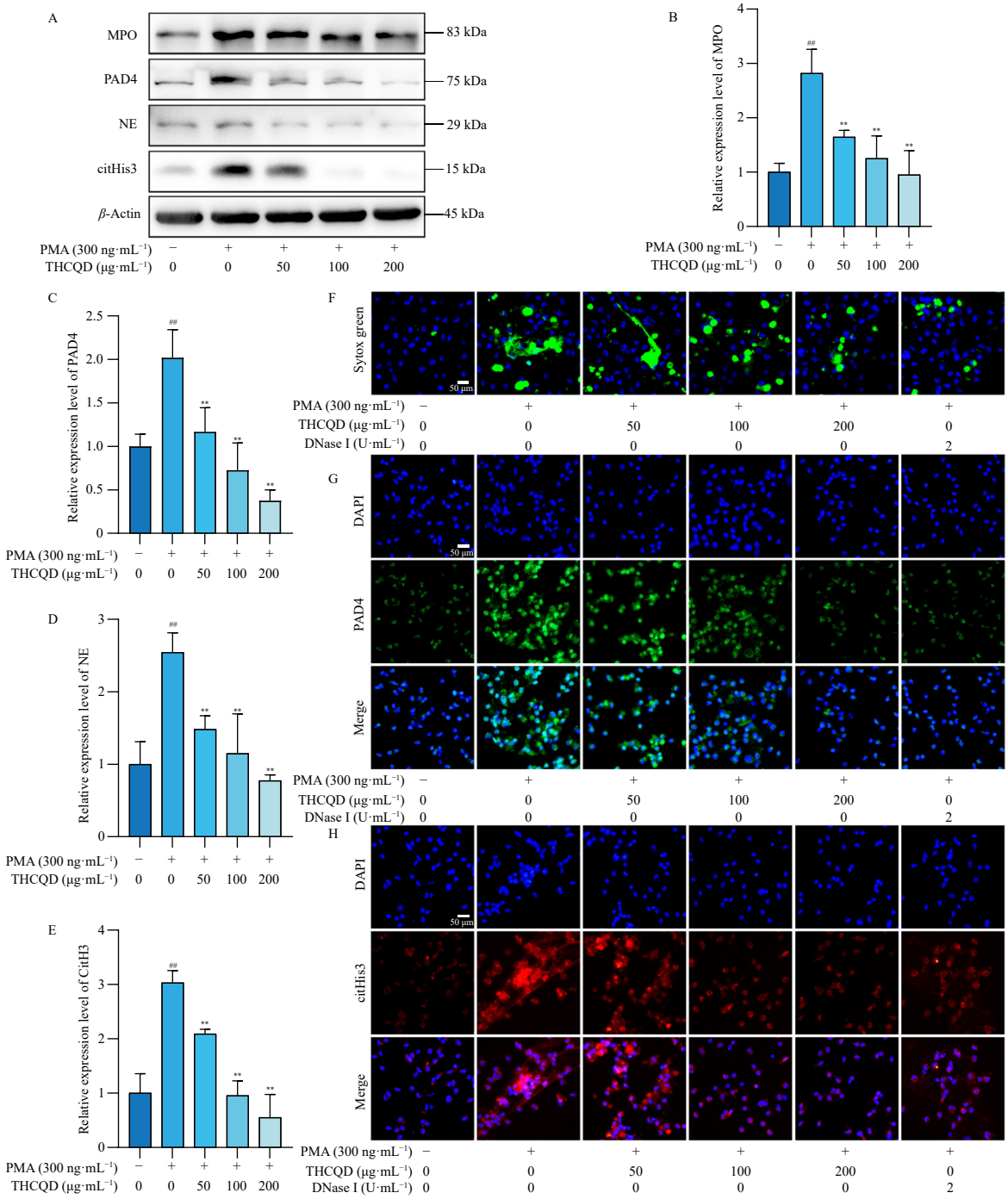

Fig. 7 THCQD inhibited PMA-induced NET formation in neutrophil-like cells *in vitro*. (A) Western blotting results analysis of key NET-associated proteins, including MPO, PAD4, NE, and citHis3, in neutrophil-like cells. (B–E) Densitometric quantification of MPO, PAD4, NE, and citHis3 protein expressions (n = 3). (F) Sytox green staining results. Scale bar, 50 μm. (G–H) Representative immunofluorescence images showing PAD4 and citHis3 localization in PMA-stimulated cells, with DAPI (blue) nuclear counterstaining. Scale bar, 50 μm. Data arepresented as the mean accompanied by the standard deviation (mean ± SD). $^{\#}P < 0.05$, $^{\#\#}P < 0.01$ *vs* control; $^{*}P < 0.05$, $^{**}P < 0.01$ *vs* PMA.

tracted from mouse bone marrow and induced with PMA demonstrated reduced NET levels and downregulated PAD4 and citHis3 expression upon THCQD treatment. These findings align with our *in vivo* experimental results. To comprehensively demonstrate THCQD's effectiveness in inhibiting NETs, we employed DNase I, a NETs inhibitor, which corroborated THCQD's inhibitory effects on NET formation.

Through an extensive literature review, we identified that PAD4 plays a crucial role in NET formation. PAD4 functions as a calcium-dependent enzyme that regulates chromatin structure and function by catalyzing the conversion of arginine residues to citrulline residues on histones [54–56]. During NET formation, PAD4-mediated citrullination facilitates chromatin depolymerization, which relaxes the chromatin structure and enables NET release, a process essential for NET formation [57–60]. An analysis using Autodock Vina was conducted to examine the interaction between PAD4 (PDB ID: 3B1T) and the active constituents within THCQD [61]. This analysis identified eight pharmacologically active compounds: glycyrrhizin, licoricesaponin H, emodin-8-glucoside, pulmatin, rhein 8-glucoside, vitexin-2-*O*-rhamnoside, gancaonin E and lindleyin. The study predicts significant binding affinity between THCQD's active components and PAD4. These findings offer novel insights into THCQD's mechanism of action on ALI and its molecular basis. While this hypothesis awaits verification through *in vitro* and *in vivo* experiments, a limitation of this paper, future studies will investigate whether these potential active

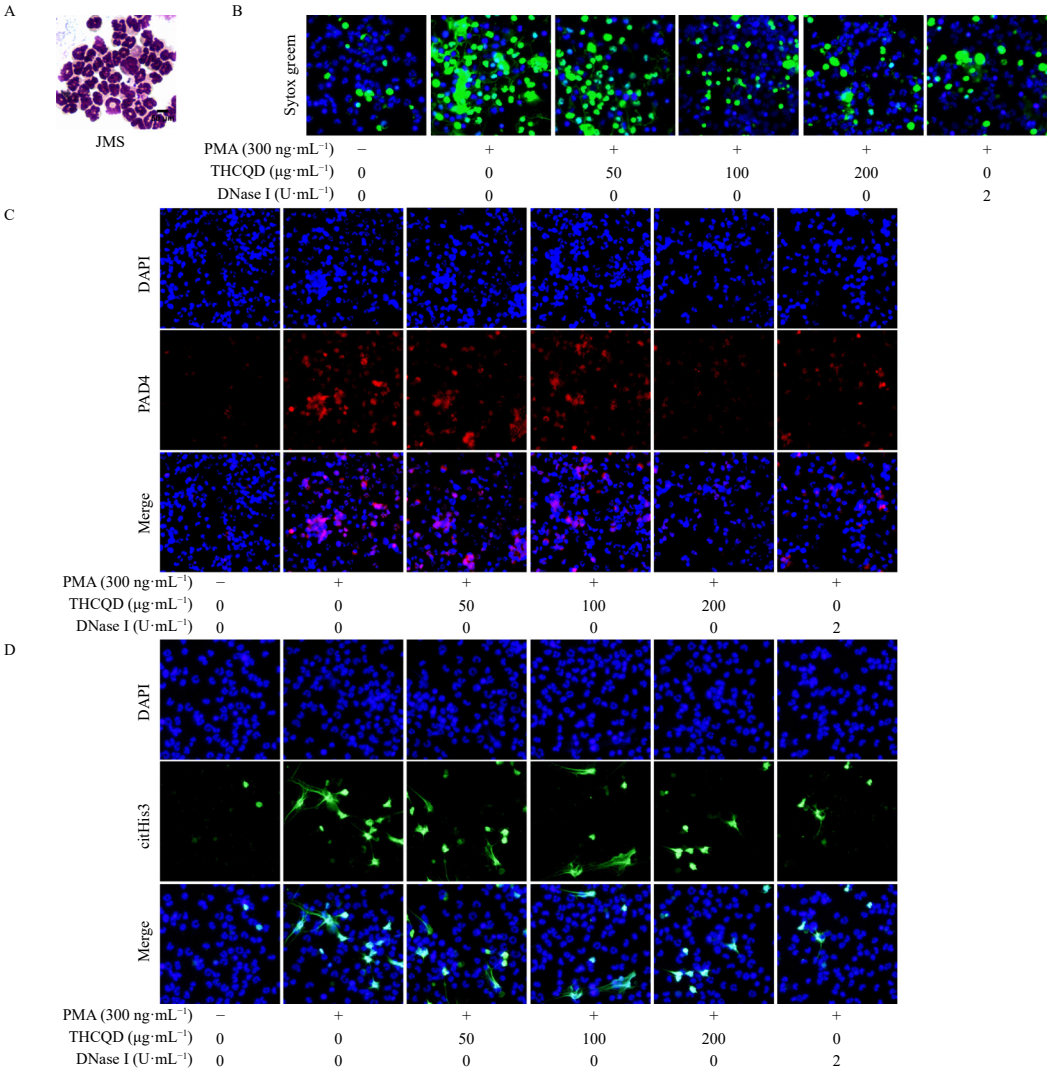

Fig. 8 THCQD inhibited PMA-induced NET formation in mouse bone marrow-derived neutrophils *in vitro*. (A) Results of Giemsa staining. Scale bar, 50 μm. (B) Sytox green staining results. Scale bar, 50 μm. (C–D) Characteristic immunofluorescence immunofluorescence images of PAD4, citHis3, and DAPI staining *in vitro*. Scale bar, 50 μm.

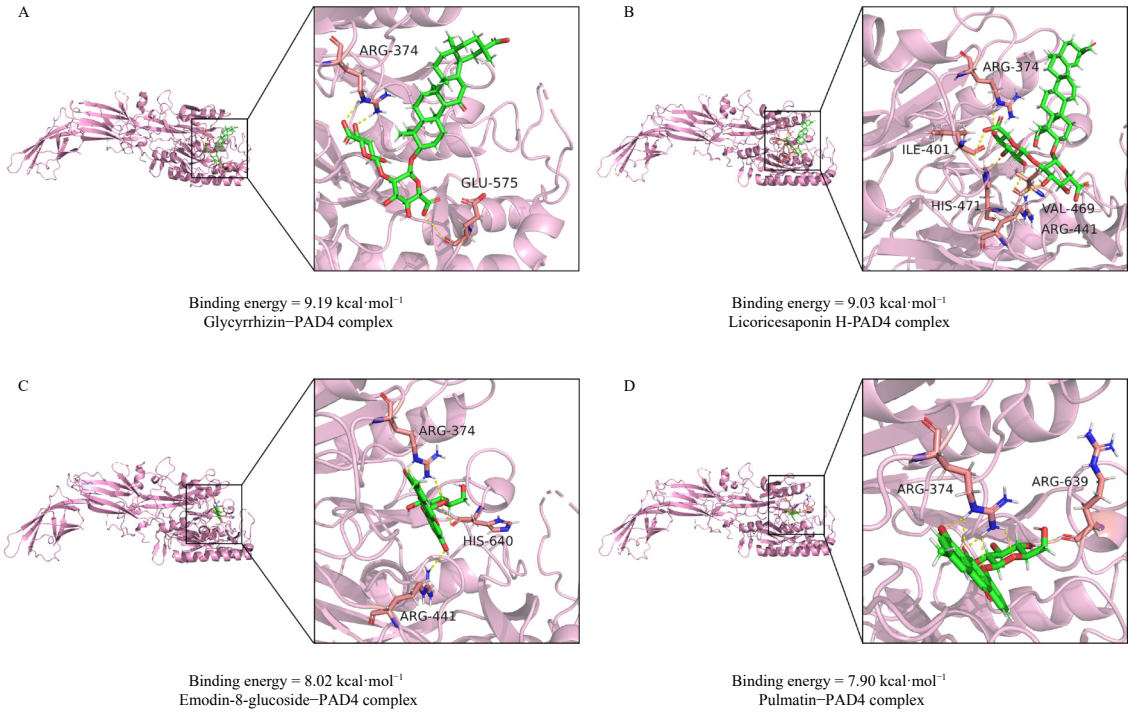

Binding energy = 9.19 kcal·mol⁻¹
Glycyrrhizin–PAD4 complex

Binding energy = 9.03 kcal·mol⁻¹
Licoricesaponin H-PAD4 complex

Binding energy = 8.02 kcal·mol⁻¹
Emodin-8-glucoside–PAD4 complex

Binding energy = 7.90 kcal·mol⁻¹
Pulmatin–PAD4 complex

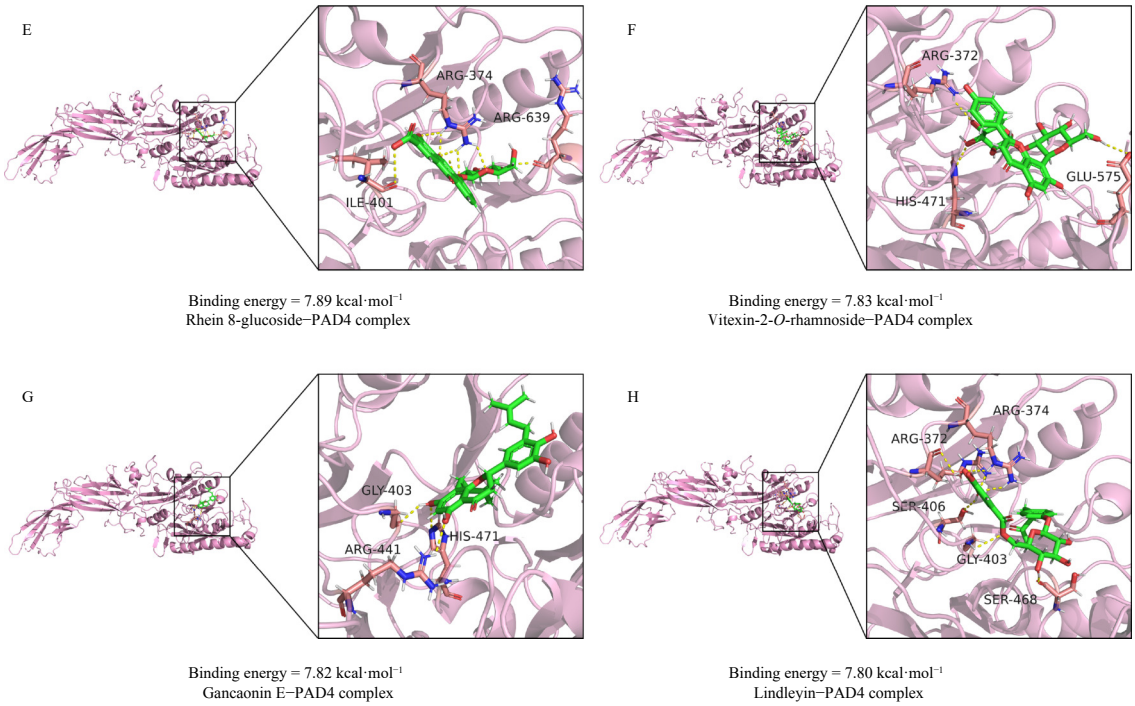

Fig. 9 THCQD can directly target PAD4. (A–H) Scoring and three-dimensional band modeling of docking of active ingredients in THCQD with PAD4.

ingredients alleviate ALI symptoms by inhibiting PAD4. This research aims to elucidate THCQD's pharmacological effects and potentially provide new strategies for ALI clinical treatment.

To thoroughly examine PAD4's function, PAD4 was overexpressed in HL-60 cells using a lentiviral-mediated method. Results demonstrated that PAD4 overexpression partially reversed THCQD's suppressive effect on NET formation. This observation highlights PAD4's critical role in THCQD's regulation of NET formation, which subsequently influences THCQD's therapeutic effect on ALI. The overexpression of PAD4 enabled a clearer understanding of PAD4's mechanism in NET formation and its molecular pathway in THCQD's potential treatment of ALI. These findings emphasize PAD4's significance in NET regulation and provide molecular evidence supporting THCQD as a potential ALI

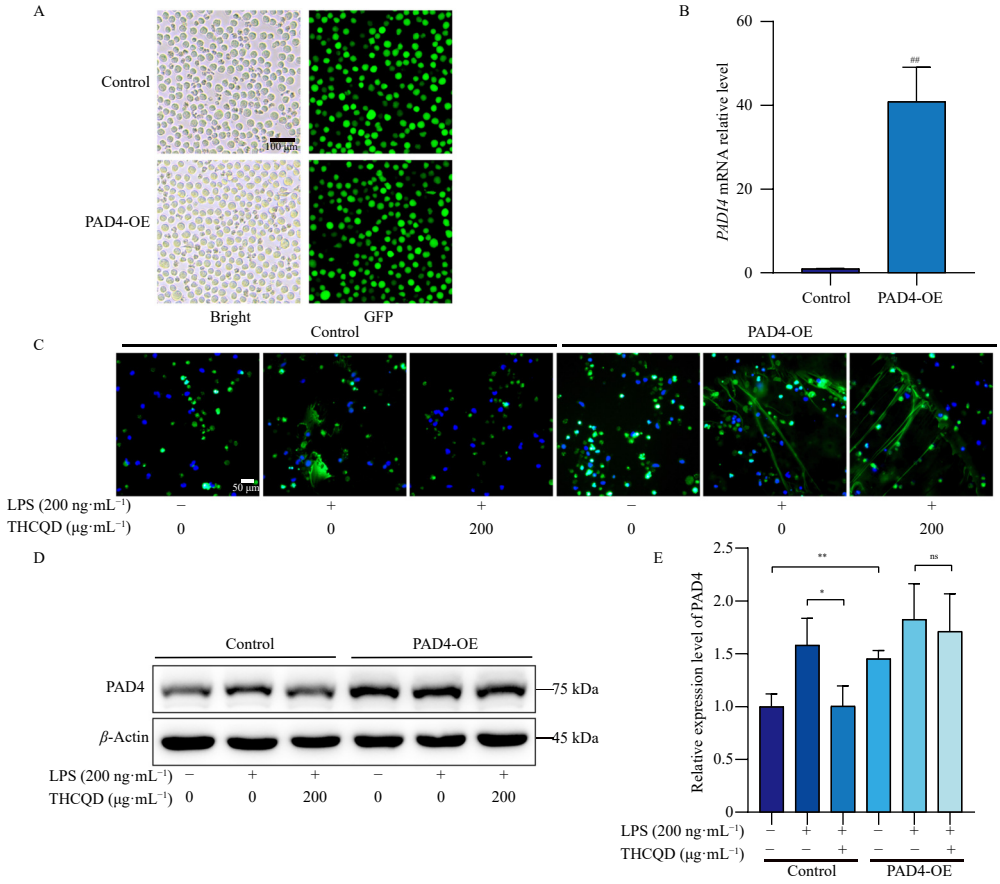

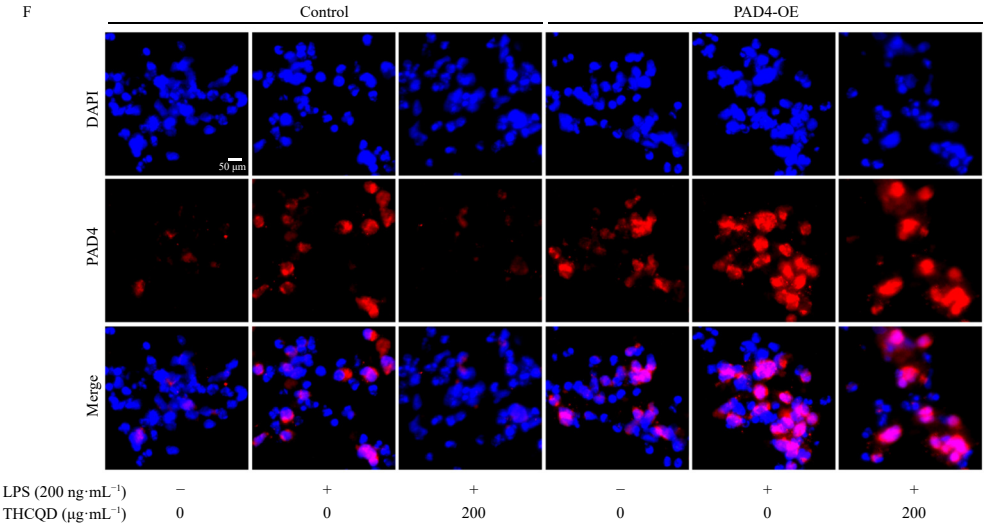

Fig. 10 Overexpression of PAD4 partially counteracted the inhibitory effect of THCQD on PAD4 formation. (A) Bright-field and GFP fluorescence images of HL-60 transfected with Lentiviral-GFP or Lentiviral-PAD4. Scale bar, 100 μm. (B) Relative *PADI4* mRNA in HL-60 expression levels in transduced HL-60 cells, quantified by qPCR (n = 3). (C) NET formation visualized using Sytox Green staining following PAD4 overexpression and THCQD (200 μg·mL^{-1}) treatment. Scale bar, 50 μm. (D–E) Western blotting analysis and densitometric quantification of PAD4 protein levels in transduced HL-60 cells treated with THCQD (200 μg·mL^{-1}) treatment determined by western blotting (n = 3). (F) Characteristic immunofluorescence images of PAD4 expression with DAPI nuclear counterstaining under the same treatment conditions. Scale bar, 50 μm. Data arepresented as the mean accompanied by the standard deviation (mean ± SD). $^{\#\#}P < 0.01$ *vs* control; $^{*}P < 0.05$, $^{**}P < 0.01$.

treatment.

5. Conclusions

This study examined THCQD's effects in treating CLP-induced ALI. THCQD significantly reduced mortality rates *in vivo*. Additionally, THCQD effectively decreased neutrophil and macrophage infiltration, suggesting anti-inflammatory properties. Notably, THCQD reduced NET formation by inhibiting PAD4, a crucial regulator in NET formation whose excessive production exacerbates lung injury. These results enhance understanding of THCQD's influence on ALI processes and reveal its molecular interactions, suggesting THCQD's potential as an effective therapeutic candidate for ALI. Consequently, these findings provide new perspectives on THCQD's underlying material foundation and additional mechanisms in ALI treatment.

Funding

This work was supporteded by the National Natural Science Foundation of China (Nos. 82374183, 82405092, 82204991, 82274246, and 82374341), the Planned Science Technology Project of Guangzhou City (Nos. 2023A03J0419 and 2023A03J0420), the General Project of Natural Science Foundation of Guangdong Province (No. 2023A1515011090), Hong Kong Scholars Program 2024 (No. XJ2024005), the Basic and Applied Basic Research Foundation of Guangdong Province (No. 2021A151510809), and the Project of Administration of Traditional Chinese Medicine of Guangdong Province of China (No. 20223013).

Declaration of competing interest

The authors declare no conflict of interest.

References

1 Liu D, Huang SY, Sun JH, et al. Sepsis-induced immunosuppression: mechanisms, diagnosis and current treatment options. *Mil Med Res*. 2022; 9(1):56. https://doi.org/10.1186/s40779-022-00422-y.
2 Mushtaq A, Kazi F. Updates in sepsis management. *Lancet Infect Dis*. 2022; 22(1):24. https://doi.org/10.1016/S1473-3099(21)00773-8.
3 Tidswell R, Inada-Kim M, Singer M. Sepsis: the importance of an accurate final diagnosis. *Lancet Respir Med*. 2021;9(1):17-18. https://doi.org/10.1016/S2213-2600(20)30520-8.
4 Kirby T. Surviving sepsis with multiple serious complications. *Lancet Respir Med*. 2023;11(4):317-318. https://doi.org/10.1016/S2213-2600(23)00078-4.
5 Fan W, Gui B, Zhou X, et al. A narrative review on lung injury: mechanisms, biomarkers, and monitoring. *Crit Care*. 2024;28(1):352. https://doi.org/10.1186/s13054-024-05149-x.
6 Liu C, Xiao K, Xie L. Progress in preclinical studies of macrophage autophagy in the regulation of ALI/ARDS. *Front Immunol*. 2022;13:922702. https://doi.org/10.3389/fimmu.2022.922702.
7 Scozzi D, Liao F, Krupnick AS, et al. The role of neutrophil extracellular traps in acute lung injury. *Front Immunol*. 2022;13:953195. https://doi.org/10.3389/fimmu.2022.953195.
8 Liu S, Su X, Pan P, et al. Neutrophil extracellular traps are indirectly triggered by lipopolysaccharide and contribute to acute lung injury. *Sci Rep*. 2016;6: 37252. https://doi.org/10.1038/srep37252.
9 Zhao J, Zhen N, Zhou Q, *et al*. NETs promote inflammatory injury by activating cGAS-STING pathway in acute lung injury. *Int J Mol Sci*. 2023; 24(6): https://doi.org/10.3390/ijms24065125.
10 Zhu S, Yu Y, Qu M, et al. Neutrophil extracellular traps contribute to immunothrombosis formation *via* the STING pathway in sepsis-associated lung injury. *Cell Death Discov*. 2023;9(1):315. https://doi.org/10.1038/s41420-023-01614-8.
11 Pan T, Lee JW. A crucial role of neutrophil extracellular traps in pulmonary infectious diseases. *Chin Med J Pulm Crit Care Med*. 2024;2(1):34-41. https://doi.org/10.1016/j.pccm.2023.10.004.
12 Kuang L, Wu Y, Shu J, et al. Pyroptotic macrophage-derived microvesicles accelerate formation of neutrophil extracellular traps *via* GSDMD-N-expressing mitochondrial transfer during sepsis. *Int J Biol Sci*. 2024;20(2): 733-750. https://doi.org/10.7150/ijbs.87646.
13 Chen L, Zhao Y, Lai D, et al. Neutrophil extracellular traps promote macrophage pyroptosis in sepsis. *Cell Death Dis*. 2018;9(6):597. https://doi.org/10.1038/s41419-018-0538-5.
14 Wang H, Kim S J, Lei Y, et al. Neutrophil extracellular traps in homeostasis and disease. *Signal Transduct Target Ther*. 2024;9(1):235. https://doi.org/10.1038/s41392-024-01933-x.
15 Jiao Y, Zhang T, Zhang C, et al. Exosomal miR-30d-5p of neutrophils induces M1 macrophage polarization and primes macrophage pyroptosis in sepsis-related acute lung injury. *Crit Care*. 2021;25(1):356. https://doi.org/10.1186/s13054-021-03775-3.
16 Linssen R S, Chai G, Ma J, et al. Neutrophil extracellular traps increase airway mucus viscoelasticity and slow mucus particle transit. *Am J Respir Cell Mol Biol*. 2021;64(1):69-78. https://doi.org/10.1165/rcmb.2020-0168OC.
17 Wu Z, Chen X, Wu S, et al. Transcriptome analysis reveals the impact of NETs activation on airway epithelial cell EMT and inflammation in bronchiolitis obliterans. *Sci Rep*. 2023;13(1):19226. https://doi.org/10.1038/s41598-023-45617-y.
18 An Y, Zhang H, Wang R, et al. Biomarkers, signaling pathways, and programmed cell death in acute lung injury and its treatment with traditional Chinese medicine: a narrative review. *Eur Rev Med Pharmacol Sci*. 2023;27(21):10157-10170. https://doi.org/10.26355/eurrev_202311_34292.
19 He YQ, Zhou CC, Yu LY, et al. Natural product derived phytochemicals in managing acute lung injury by multiple mechanisms. *Pharmacol Res*. 2021;163:105224. https://doi.org/10.1016/j.phrs.2020.105224.
20 Dong JY, Yin HL, Hao H, et al. Research progress on autophagy regulation by active ingredients of traditional Chinese medicine in the treatment of acute lung injury. *J Inflamm Res*. 2023;16:1671-1691. https://doi.org/10.2147/JIR.

S398203.
21 Lu SM, Yang B, Tan ZB, et al. TaoHe ChengQi decoction ameliorates sepsis-induced cardiac dysfunction through anti-ferroptosis *via* the Nrf2 pathway. *Phytomedicine*. 2024;129:155597. https://doi.org/10.1016/j.phymed.2024.155597.
22 Yuan Z, Qiao H, Wang Z, et al. Taohe Chengqi decoction alleviated metabolic-associated fatty liver disease by boosting branched chain amino acids catabolism in the skeletal muscles of type 2 diabetes mellitus. *Phytomedicine*. 2024;126:155315. https://doi.org/10.1016/j.phymed.2023.155315.
23 Zhou S, Ai Z, Li W, et al. Deciphering the pharmacological mechanisms of Taohe-Chengqi decoction extract against renal fibrosis through integrating network pharmacology and experimental validation *in vitro* and *in vivo*. *Front Pharmacol*. 2020;11:425. https://doi.org/10.3389/fphar.2020.00425.
24 Deng M, Chen S, Wu J, et al. Exploring the anti-inflammatory and immune regulatory effects of Taohe Chengqi decoction in sepsis-induced lung injury. *J Ethnopharmacol*. 2024;333:118404. https://doi.org/10.1016/j.jep.2024.118404.
25 Gu J, Ran X, Deng J, et al. Glycyrrhizin alleviates sepsis-induced acute respiratory distress syndrome *via* suppressing of HMGB1/TLR9 pathways and neutrophils extracellular traps formation. *Int Immunopharmacol*. 2022;108:108730. https://doi.org/10.1016/j.intimp.2022.108730.
26 Wu D, Spencer CB, Ortoga L, et al. Histone lactylation-regulated METTL3 promotes ferroptosis *via* m6A-modification on ACSL4 in sepsis-associated lung injury. *Redox Biol*. 2024;74:103194. https://doi.org/10.1016/j.redox.2024.103194.
27 Ruiz S, Vardon-Bounes F, Merlet-Dupuy V, et al. Sepsis modeling in mice: ligation length is a major severity factor in cecal ligation and puncture. *Intensive Care Med Exp*. 2016;4(1):22. https://doi.org/10.1186/s40635-016-0096-z.
28 Shen W, Gan J, Xu S, et al. Penehyclidine hydrochloride attenuates LPS-induced acute lung injury involvement of NF-*κ*B pathway. *Pharmacol Res*. 2009;60(4):296-302. https://doi.org/10.1016/j.phrs.2009.04.007.
29 Yehya N, Xin Y, Oquendo Y, et al. Cecal ligation and puncture accelerates development of ventilator-induced lung injury. *Am J Physiol Lung Cell Mol Physiol*. 2015;308(5):L443-L451. https://doi.org/10.1152/ajplung.00312.2014.
30 Papayannopoulos V. Neutrophil extracellular traps in immunity and disease. *Nat Rev Immunol*. 2018;18(2):134-147. https://doi.org/10.1038/nri.2017.105.
31 Qu M, Chen Z, Qiu Z, et al. Neutrophil extracellular traps-triggered impaired autophagic flux *via* METTL3 underlies sepsis-associated acute lung injury. *Cell Death Discov*. 2022;8(1):375. https://doi.org/10.1038/s41420-022-01166-3.
32 He L, Liu R, Yue H, et al. Interaction between neutrophil extracellular traps and cardiomyocytes contributes to atrial fibrillation progression. *Signal Transduct Target Ther*. 2023;8(1):279. https://doi.org/10.1038/s41392-023-01497-2.
33 Wang R, Zhu Y, Liu Z, et al. Neutrophil extracellular traps promote tPA-induced brain hemorrhage *via* cGAS in mice with stroke. *Blood*. 2021;138(1):91-103. https://doi.org/10.1182/blood.2020008913.
34 Yazdani H O, Roy E, Comerci A J, et al. Neutrophil extracellular traps drive mitochondrial homeostasis in tumors to augment growth. *Cancer Res*. 2019;79(21):5626-5639. https://doi.org/10.1158/0008-5472.CAN-19-0800.
35 Chen H, Luo M, Wang X, et al. Inhibition of PAD4 enhances radiosensitivity and inhibits aggressive phenotypes of nasopharyngeal carcinoma cells. *Cell Mol Biol Lett*. 2021;26(1):9. https://doi.org/10.1186/s11658-021-00251-2.
36 Clark HL, Abbondante S, Minns MS, et al. Protein deiminase 4 and CR3 regulate aspergillus fumigatus and *β*-glucan-induced neutrophil extracellular trap formation, but hyphal killing is dependent only on CR3. *Front Immunol*. 2018;9:1182. https://doi.org/10.3389/fimmu.2018.01182.
37 Bukong TN, Cho Y, Iracheta-Vellve A, et al. Abnormal neutrophil traps and impaired efferocytosis contribute to liver injury and sepsis severity after binge alcohol use. *J Hepatol*. 2018;69(5):1145-1154. https://doi.org/10.1016/j.jhep.2018.07.005.
38 Han F, Ding ZF, Shi XL, et al. Irisin inhibits neutrophil extracellular traps formation and protects against acute pancreatitis in mice. *Redox Biol*. 2023;64:102787. https://doi.org/10.1016/j.redox.2023.102787.
39 Hsieh YT, Chou YC, Kuo PY, et al. Down-regulated miR-146a expression with increased neutrophil extracellular traps and apoptosis formation in autoimmune-mediated diffuse alveolar hemorrhage. *J Biomed Sci*. 2022;29(1):62. https://doi.org/10.1186/s12929-022-00849-4.
40 Brings C, Frobel J, Cadeddu P, et al. Impaired formation of neutrophil extracellular traps in patients with MDS. *Blood Adv*. 2022;6(1):129-137. https://doi.org/10.1182/bloodadvances.2021005721.
41 Liu B, Wang Z, He R, et al. Buformin alleviates sepsis-induced acute lung injury *via* inhibiting NLRP3-mediated pyroptosis through an AMPK-dependent pathway. *Clin Sci (Lond)*. 2022;136(4):273-289. https://doi.org/10.1042/CS20211156.
42 Wang L, Tang Y, Tang J, et al. Endothelial cell-derived extracellular vesicles expressing surface VCAM1 promote sepsis-related acute lung injury by targeting and reprogramming monocytes. *J Extracell Vesicles*. 2024;13(3):e12423. https://doi.org/10.1002/jev2.12423.
43 Park I, Kim M, Choe K, *et al*. Neutrophils disturb pulmonary microcirculation in sepsis-induced acute lung injury. *Eur Respir J*. 2019;53(3):1800786. https://doi.org/10.1183/13993003.00786-2018.
44 Chen R, Cao C, Liu H, et al. Macrophage Sprouty4 deficiency diminishes sepsis-induced acute lung injury in mice. *Redox Biol*. 2022;58:102513. https://doi.org/10.1016/j.redox.2022.102513.
45 Zhuang C, Kang M, Lee M. Delivery systems of therapeutic nucleic acids for the treatment of acute lung injury/acute respiratory distress syndrome. *J Control Release*. 2023;360:1-14. https://doi.org/10.1016/j.jconrel.2023.06.018.
46 Bos L, Ware L B. Acute respiratory distress syndrome: causes, pathophysiology, and phenotypes. *Lancet*. 2022;400(10358):1145-1156. https://doi.org/10.1016/S0140-6736(22)01485-4.
47 Shang L, Zhang M, Li J, et al. Dachengqi decoction alleviates acute lung injury by suppressing HIF-1α-mediated glycolysis. *J Ethnopharmacol*. 2024;321:117410. https://doi.org/10.1016/j.jep.2023.117410.
48 Zhu Y, Li J, Pang Z. Recent insights for the emerging COVID-19: Drug discovery, therapeutic options and vaccine development. *Asian J Pharm Sci*. 2021;16(1):4-23. https://doi.org/10.1016/j.ajps.2020.06.001.
49 Wu J, Lan Y, Wu J, et al. Sepsis-induced acutelung injury is alleviated by small molecules from dietary plants *via* pyroptosis modulation. *J Agric Food Chem*. 2023;71(32):12153-12166. https://doi.org/10.1021/acs.jafc.2c08926.
50 Xu H, Xu J, Xu L, et al. Interleukin-33 contributes to ILC2 activation and early inflammation-associated lung injury during abdominal sepsis. *Immunol Cell Biol*. 2018;96(9):935-947. https://doi.org/10.1111/imcb.12159.
51 Zhao R, Lopez B, Schwingshackl A, et al. Protection from acute lung injury by a peptide designed to inhibit the voltage-gated proton channel. *Iscience*. 2023;26(1):105901. https://doi.org/10.1016/j.isci.2022.105901.
52 Wang Y, Shi C, Guo J, et al. IDH1/MDH1 deacetylation promotes acute liver failure by regulating NETosis. *Cell Mol Biol Lett*. 2024;29(1):8. https://doi.org/10.1186/s11658-023-00529-7.
53 Lee YS, Kang SU, Lee MH, et al. GnRH impairs diabetic wound healing through enhanced NETosis. *Cell Mol Immunol*. 2020;17(8):856-864. https://doi.org/10.1038/s41423-019-0252-y.
54 Mikacenic C, Moore R, Dmyterko V, et al. Neutrophil extracellular traps (NETs) are increased in the alveolar spaces of patients with ventilator-associated pneumonia. *Crit Care*. 2018;22(1):358. https://doi.org/10.1186/s13054-018-2290-8.
55 Zhang H, Wang Y, Qu M, et al. Neutrophil, neutrophil extracellular traps and endothelial cell dysfunction in sepsis. *Clin Transl Med*. 2023;13(1):e1170. https://doi.org/10.1002/ctm2.1170.
56 Lewis HD, Liddle J, Coote JE, et al. Inhibition of PAD4 activity is sufficient to disrupt mouse and human NET formation. *Nat Chem Biol*. 2015;11(3):189-191. https://doi.org/10.1038/nchembio.1735.
57 Thiam HR, Wong SL, Qiu R, et al. NETosis proceeds by cytoskeleton and endomembrane disassembly and PAD4-mediated chromatin decondensation and nuclear envelope rupture. *Proc Natl Acad Sci USA*. 2020;117(13):7326-7337. https://doi.org/10.1073/pnas.1909546117.
58 Thiam HR, Wong SL, Wagner DD, et al. Cellular mechanisms of NETosis. *Annu Rev Cell Dev Biol*. 2020;36:191-218. https://doi.org/10.1146/annurev-cellbio-020520-111016.
59 Guo W, Gong Q, Zong X, et al. GPR109A controls neutrophil extracellular traps formation and improve early sepsis by regulating ROS/PAD4/Cit-H3 signal axis. *Exp Hematol Oncol*. 2023;12(1):15. https://doi.org/10.1186/s40164-023-00376-4.
60 Zhu YP, Speir M, Tan Z, et al. NET formation is a default epigenetic program controlled by PAD4 in apoptotic neutrophils. *Sci Adv*. 2023;9(51):eadj1397. https://doi.org/10.1126/sciadv.adj1397.
61 Jiang L, Yang D, Zhang Z, et al. Elucidating the role of *Rhodiola rosea* L. in sepsis-induced acute lung injury *via* network pharmacology: emphasis on inflammatory response, oxidative stress, and the PI3K-AKT pathway. *Pharm Biol*. 2024;62(1):272-284. https://doi.org/10.1080/13880209.2024.2319117.